International Journal of Microwave and Wireless Technologies

cambridge.org/mrf

Analysis and empirical modeling of rain clutter for automotive radar validation

Sonakshi Gupta[1], Isabella Varga[2], Matthias A. Hein[2] and Thomas Dallmann[1]

[1]Radio Technologies for Automated and Connected Vehicles Research Group at Thüringer Innovationszentrum Mobilität, Technische Universität Ilmenau, Ilmenau, Germany and [2]RF and Microwave Research Group at Thüringer Innovationszentrum Mobilität, Technische Universität Ilmenau, Ilmenau, Germany

Research Paper

Cite this article: Gupta S, Varga I, Hein MA, Dallmann T (2026) Analysis and empirical modeling of rain clutter for automotive radar validation. *International Journal of Microwave and Wireless Technologies* **18**(3), 401–408. https://doi.org/10.1017/S1759078726103055

Received: 30 September 2025
Revised: 18 February 2026
Accepted: 22 February 2026
First published online: 9 March 2026

Keywords:
automotive radar; empirical model; Millimeter wave; Probability distribution function; rain clutter

Corresponding author: Sonakshi Gupta; Email: sonakshi.gupta@tu-ilmenau.de

Abstract

Simulation of precipitation for automotive radar validation requires suitable rain clutter models to test radars against various weather conditions. Although there have been developments in the investigation of attenuation due to rain, rain back-scattering needs to be explored further. However, the analytical modeling is challenging. Even if the raindrops are considered perfect conducting spheres, the Rayleigh approximation cannot be used to calculate RCS since rain droplets are comparable to automotive radar wavelengths. Therefore, reflectivity measurements at different rain rates were conducted in an indoor rain facility. Based on the measured data, reflectivity from rain back-scattering for automotive radars is modeled using an empirical approach. The results indicate that reflectivity can be modeled using an inverse-gamma or inverse-Weibull distribution parametrized by rain rate, and that the observed distribution varies with the spatial range considered, highlighting the impact of range-dependent effects on rain clutter modeling.

Introduction

Millimeter-wave radar systems are indispensable to the advanced driving assistance systems (ADAS) sensor suite. Radars can detect targets in adverse weather conditions, where cameras and LiDAR are often rendered ineffective due to limited visibility. This paper analyzes radars operating at 77–81 GHz. An earlier version of it was presented at the 19th Conference of Antennas and Propagation (EuCAP 2025) and published in its proceedings [1].

Precipitation can significantly impact automotive radar performance due to scattering, absorption, diffraction, and depolarization effects. This leads to signal attenuation and a reduced dynamic range, which can cause ghost targets. Therefore, understanding how precipitation scattering affects radars and developing suitable models allows us to evaluate the limitations of these radars. However, physical road tests in varying weather conditions are unpredictable and not reproducible. Hence, virtual testing to simulate real-world scenarios is a more practical solution.

Radar target emulators, together with software, hardware, and vehicle-in-the-loop (SiL/HiL/ViL) test setups, provide controlled and repeatable environments for evaluating radar sensors and perception algorithms [2–5]. To realistically include rain effects in such frameworks, precipitation must first be understood and modeled as an isolated physical phenomenon. This avoids confounding influences such as wind or multipath propagation, which can be better addressed in dedicated future studies. Treating precipitation effect independently allows it to be flexibly overlaid onto existing radar scenarios. Accordingly, this paper models rain back-scatter clutter using an empirical approach suitable for virtual radar simulations.

Related work

Mie theory

Mie scattering theory describes the dependence of the radar cross-section (RCS) σ of a spherical particle on the ratio of its size to the radar wavelength λ [6]. As depicted in Figure 1, it can be classified into three scattering regions. In the Rayleigh region, the size of the sphere is much smaller than the wavelength. In the resonant region, the size of the sphere is in the order of the wavelength, and in the optical region, the size of the sphere is much larger than the wavelength. Precipitation particles, such as raindrops, range in size from approximately 0.1 to 8 mm [7]; the size parameter can be calculated for automotive radars. Based on their frequency band and the size of rain droplets, they cover two scattering regions. This makes it unsuitable to apply Rayleigh, resonant, or optical approximations individually.

© The Author(s), 2026. Published by Cambridge University Press in association with The European Microwave Association

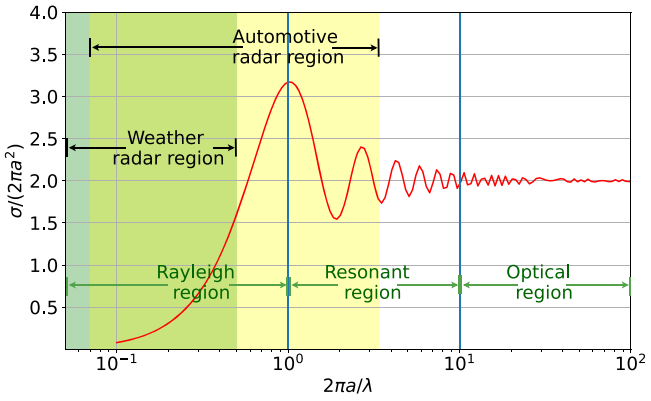


Figure 1. Perfect conductor sphere scattering (radius a).

Automotive radars

Current papers on precipitation in automotive radar technology focus on attenuation occurring due to forward scattering. As referred from the ITU-R P.838 model [8, 9],

$$A = aR^b \tag{1}$$

expresses a power-law relationship, specifying rain attenuation. Here, A is attenuation in dB/km, R is rain rate in mm/h, and coefficients a and b depend on transmission frequency and atmospheric temperature. These coefficients have been derived through logarithmic regression and Mie scattering calculation. However, as mentioned in [10], this relation is most accurate for the X- to K-band frequency range. Also, attenuation for automotive radar operating at 77 GHz for rain rates up to 100 mm/h over their maximum range of 350 m is approximately 11 dB [11]. Despite the extreme rain rates at the maximum range, the attenuation remains relatively modest and does not significantly affect the operational capability of the radar.

Moreover, back-scattering caused by precipitation incites an increase in clutter level in the received signal, which reduces dynamic range and can lead to ghost targets. There have been some recent developments in the investigation of rain clutter for automotive radar. [11, 12] discuss the effect of rain attenuation on target detection. Additionally, in [13], experiments were conducted with 9.375, 35, 70, and 95 GHz radars to measure rain back-scattering and develop its macroscopic power-law relationship with rainfall rate. The study utilized outdoor measurements and primarily served to verify fundamental Mie scattering physics. Also, the rain clutter modeling for E-band radars remains largely unexplored. Therefore, this paper aims to comprehensively investigate and develop an empirical statistical model of back-scattering from precipitation clutter for 77–81 GHz radars.

Back-scattering can be characterized by the RCS, which is the power density reflected by a target in relation to the power density radiated by the radar's transmitter antenna in the target vicinity. For volumetric targets, such as rain droplets, RCS in m^2 can be further expressed as [6]

$$\sigma = \eta V \tag{2}$$

Here, η is the clutter reflectivity factor in m^{-1} and V is the volume illuminated by the radar within a particular range in m^3. Rain reflectivity is a function of raindrop size distribution and back-scattering from each raindrop. This paper attempts to model η for different rain rates based on measured data. The measurement setup is explained in detail in the third section, followed by the analysis of the measured data in the fourth section. Results are discussed in the fifth section and summarized in the sixth section.

Measurement setup

Measurements were conducted at the CARISSMA Research Center in Ingolstadt, Germany [14], which is a controlled indoor facility. It has an asphalt track with road markings and a concrete divider covered by microwave absorbers on one side, as shown in Figure 2. A 50 m long irrigation system is installed above the track, producing adjustable rain intensity and drop size distribution. Rain for the measurements was generated at rain rates of 16, 32, 66, and 98 mm/h, which all follow the corresponding Marshall–Palmer rain distribution and thus resemble realistic rainfall [15].

The measurements were conducted for two setups, the first one with a triple reflector (TR) and the second one without TR and therefore agreeing with a background (BG) measurement. The TR was measured at 20, 30, 40, and 50 m and supplemented by a corresponding BG measurement for each given rain rate except 98 mm/h. For 98 mm/h, only measurements at 30 m were taken. Data was recorded with the Continental 77 GHz radar sensor ARS430 [16]. The radar sensor provides a detection list with RCS in dBsm, azimuth angles in rad, time stamps in ms (Coordinated Universal Time) and range bins in m.

Methodology

This paper analyzes measurements for TR and BG setups at distances of 20, 30, 40, and 50 m at rain rates of 16, 32, and 66 mm/h, as well as 30 m at a 98 mm/h rain rate. In total, 26 measurements were analyzed, each referred to as a scenario in the following.

Based on the azimuth and elevation half-power beamwidth of the radar antenna, the elliptical frustum volume for each range cell is calculated to obtain the rain reflectivity, η:

$$V = \frac{\pi}{3} \tan\left(\frac{\phi_\Delta}{2}\right) \tan\left(\frac{\theta_\Delta}{2}\right) \left(\frac{r_\Delta^3}{4} + 3r_\Delta r^2\right) \tag{3}$$

Here, V is the volume in m^3, ϕ_Δ is the half-power beamwidth in the azimuth (horizontal) direction in rad, θ_Δ is the half-power beamwidth in the elevation (vertical) direction in rad, r_Δ is the range resolution in m, and r is the measured range bin of the target region in m.

Data outside the defined area under test ($R_{y_{min}}^{y_{max}}$), restricted to $x \in [-2.5\text{ m},\ 2.5\text{ m}]$ and $y \in [y_{\min},\ y_{\max}]$, were discarded to avoid reflections from the ceiling, walls, and a concrete divider (see Figure 2). The reference model is based on the y-axis observation range of $y \in [10\text{ m},\ 20\text{ m}]$, hereafter referred to as R_{10}^{20}. In addition, three alternative $R_{y_{min}}^{y_{max}}$ ranges were analyzed: R_{10}^{11} with $y \in [10\text{ m},\ 11\text{ m}]$, R_{10}^{15} with $y \in [10\text{ m},\ 15\text{ m}]$, and R_{10}^{30} with $y \in [10\text{ m},\ 30\text{ m}]$.

The rain back-scattering clutter model is primarily based on R_{10}^{20}, as it provides a sufficient detection density along its whole range. Since the number of raindrop detections by automotive radar decreases with increasing distance from the sensor, R_{10}^{20} serves as a suitable reference. Nevertheless, to investigate the influence of spatial configuration, additional $R_{y_{min}}^{y_{max}}$ ranges were also analyzed.

https://doi.org/10.1017/S1759078726103055 Published online by Cambridge University Press

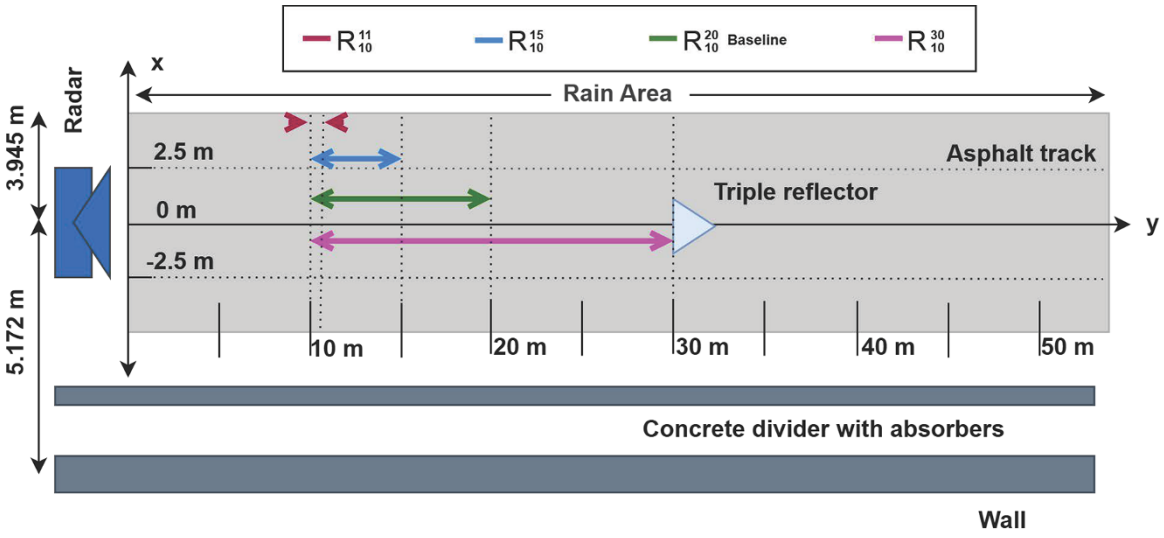


Figure 2. Measurement setup at CARISSMA.

Table 1. Sample statistics of different scenarios with the overall mean computed over the full data set

Scenario	Rain rate (mm/h)	Skewness	Outlier percentage	Mean	Median	Std. dev.
BG	16	7.2496	1.8483	0.000225	0.000112	0.000474
TR: 40 m	32	5.3015	1.3821	0.000264	0.000185	0.000285
BG	66	6.6135	2.1047	0.000785	0.000327	0.002424
TR: 30 m	98	8.8427	2.0178	0.000927	0.000398	0.002928
Mean (all data)		**10.65**	**1.52**	**0.000422**	**0.000216**	**0.00212**

Adaptive binning

A histogram was created for each scenario to model the data empirically. Table 1 presents the sample statistics. The distributions are strongly skewed (skewness 5.3–8.8, overall mean > 10), indicating heavy tails across all rain rates. The outliers comprise only around 1–2% (with an overall mean $< 2\%$) of the data, yet they strongly affect the statistical histograms. Such characteristics show that fixed-width binning is ineffective. The strong skewness and sparse but extreme outliers force most low values into a very few bins, thereby flattening the higher range. Therefore, adaptive binning is required to preserve detail in dense regions while still accounting for outliers.

In earlier work [1], this issue was addressed by removing 0.1% outliers prior to applying fixed-width binning. In contrast, the present work employs a robust adaptive binning strategy, which mitigates the impact of outliers more effectively and eliminates the need for outlier filtering. The binning approach follows a hierarchical decision process in which only one binning rule is ultimately applied, depending on the statistical characteristics of the data.

Freedman–Diaconis rule

As per Freedman–Diaconis (FD), the interquartile range (IQR) is a pragmatic measure of spread, where

$$\text{Bin width} = 2\,\frac{\text{IQR}}{n^{1/3}} \tag{4}$$

Freedman and Diaconis introduced it in [17]. Here, IQR refers to the data range between the first and third quartiles (Q1 and Q3). If this produces at least 80% of the desired number of bins (i.e., 500), it complies with the structure of the dense region by IQR resistance to outliers and yields enough resolution, so no further adjustment is needed and the algorithm terminates.

Log adaptive rule

If the FD IQR 25–75 rule produces substantially fewer bins than required, the absolute skewness of the data is evaluated. When the skewness exceeds a threshold of 3, and all values are positive, logarithmic binning is applied. The bins are spaced uniformly in the logarithmic domain and then mapped back to the linear scale. Logarithmic binning is well-suited for long-tailed or power-law distributions [18], as it preserves resolution in dense regions while compressing the tail.

Modified FD rule

If the skewness does not exceed the threshold, a fallback method based on a modified FD rule is used. This method computes the bin widths from the data range between the 15th and 85th percentiles, thereby ignoring the most extreme 15% of values on each tail. The resulting bin widths are then applied to the full data range.

Figure 3 illustrates example histograms of the different datasets utilizing the different binning methods, showing η on the x-axis and the density of occurrence per bin on the y-axis. Depending on the data characteristics, a different adaptive binning rule is selected, and one representative example of each case is shown. To assess the uniformity of the data distribution across histogram bins, the

https://doi.org/10.1017/S1759078726103055 Published online by Cambridge University Press

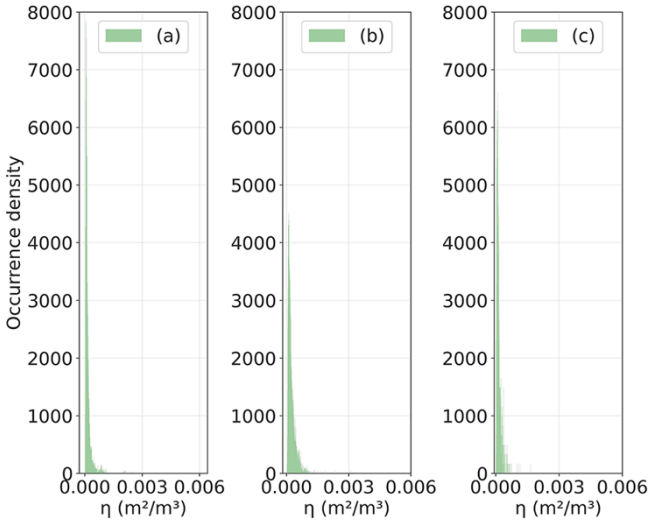


Figure 3. Histograms with adaptive binning methods: (a) rain rate: 16 mm/h, scenario: TR 40 m, binning: FD IQR 25–75, (b) rain rate: 32 mm/h, scenario: TR 30 m, binning: log adaptive, and (c) rain rate: 16 mm/h, scenario: BG, binning: modified FD IQR 15-85.

Shannon entropy is computed as

$$H = -\sum_i p_i \log p_i, \tag{5}$$

Here, p_i denotes the empirical bin probabilities [19]. The entropy is normalized to $[0, 1]$, with higher values indicating more uniform bin occupancy. Fixed-width binning yields an average entropy of 0.564. Among the individual adaptive rules, the FD rule based on the 25–75 IQR results in 0.557, log-adaptive binning yields 0.564, and the modified FD rule using the 15–85 IQR achieves the highest average entropy of 0.663. The proposed adaptive binning approach, which selects between these methods based on data characteristics, attains an average entropy of 0.592 and outperforms individual strategies in certain cases, indicating improved robustness across datasets.

The distinct shape of the distribution, with a steep rise followed by a heavily skewed tail, necessitates an investigation to reproduce this behavior most effectively. The objective is to identify a model that optimally fits the data. To this end, the datasets were fitted with 119 probability distributions available in the SciPy statistics library [20]. To achieve this, hyper parameters were calculated based on the data set properties and used in an exhaustive grid search to identify a list of local minima. This list was then used to initialize the Levenberg-Marquardt optimization algorithm [21] to obtain optimized parameters for all the probability distribution fittings.

Probability distribution functions

The key probability distributions with the most relevance are given together with a description and their probability density function (pdf) below [22].

Rayleigh distribution

The Rayleigh distribution is commonly used to model the magnitude of a vector with normally distributed components and for stochastic modeling of RCS in Swerling models III and IV [23]. Its pdf is given by

$$f(x;\varsigma) = \frac{x}{\varsigma^2} e^{-\frac{x^2}{2\varsigma^2}}, \quad x \geq 0 \tag{6}$$

Here $\varsigma > 0$ is the scale parameter.

Exponential distribution

The exponential distribution is commonly used to model the time until the next event occurs, under the assumption that events take place at a constant average rate. It is also applied in stochastic modeling of RCS within the Swerling I and II models [23, 24]. Its pdf is given by

$$f(x;\lambda) = \lambda e^{-\lambda x}, \quad x \geq 0, \tag{7}$$

where $\lambda > 0$ is the rate parameter.

Furthermore, if the Rayleigh distribution is defined as $R \sim \text{Rayleigh}(\sigma)$, then its square $E = R^2$ follows an exponential distribution. This implies that when the amplitude R of the received radar signal is Rayleigh distributed, the corresponding power, which is proportional to R^2, follows an exponential distribution.

Rician distribution

The Rician distribution describes the magnitude of a circularly symmetric normal random variable, often used in signal processing to describe fading channels. It generalizes the Rayleigh distribution by introducing a non-centrality parameter [25]. Its pdf is given by:

$$f(x;\nu,\varsigma) = \frac{x}{\varsigma^2} e^{-\frac{(x^2+\nu^2)}{2\varsigma^2}} \mathrm{I}_0\left(\frac{x\nu}{\varsigma^2}\right), \quad x \geq 0 \tag{8}$$

Here ν is the non-centrality parameter, ς is the scale parameter, and I_0 is the modified Bessel function of the first kind.

Weibull distribution

The Weibull distribution is a versatile distribution employed in reliability engineering, life data analysis, and modeling failure times. It generalizes the exponential distribution by introducing a shape parameter. Its pdf is given by

$$f(x;\lambda,k) = \frac{k}{\lambda}\left(\frac{x}{\lambda}\right)^{k-1} e^{-\left(\frac{x}{\lambda}\right)^k}, \quad x \geq 0 \tag{9}$$

Here $\lambda > 0$ is the scale and $k > 0$ is the shape parameter.

Gamma distribution

The gamma distribution generalizes the exponential distribution and is commonly required to model waiting times or the sum of independent exponentially distributed random variables. Its pdf is given by

$$f(x;\alpha,\beta) = \frac{\beta^\alpha x^{\alpha-1} e^{-\beta x}}{\Gamma(\alpha)}, \quad x \geq 0 \tag{10}$$

Here $\alpha > 0$ is the shape parameter, $1/\beta > 0$ is the scale parameter, and $\Gamma(\alpha)$ is the gamma function. The gamma distribution can also be defined in terms of the shape parameter (α) and the rate parameter (β), where the rate is the reciprocal of the scale parameter.

Inverse-Weibull (IW) distribution

The inverse-Weibull (IW) distribution is obtained by taking the reciprocal of a Weibull-distributed variable. If a random variable W follows a Weibull distribution with shape parameter k and scale parameter λ, given by $W \sim \text{Weibull}(k, \lambda)$, then the reciprocal

https://doi.org/10.1017/S1759078726103055 Published online by Cambridge University Press

$Y = 1/W$ follows an IW distribution characterized by the same shape k and scale λ. Its pdf is [26, 27].

$$f(x;k,\lambda) = \frac{k}{\lambda^k} x^{-k-1} e^{-(\frac{\lambda}{x})^k}, \quad x > 0 \tag{11}$$

Here, $k > 0$ controls the shape of the distribution, and $\lambda > 0$ is the scale parameter. Moreover, it can be noted that a random variable W following the Weibull distribution can also be considered a linearization of its reciprocal $Y = 1/W$, in the sense that the reciprocal can be described by the first-order term of a Taylor expansion.

Inverse-gamma (IG) distribution

The inverse-gamma (IG) distribution is a probability distribution of a variable's reciprocal that follows a gamma distribution. If a random variable X follows a gamma distribution with shape parameter α and rate parameter β (so that its scale is $1/\beta$), denoted $X \sim \text{Gamma}(\alpha, \beta)$, then the reciprocal variable $Y = 1/X$, follows an IG distribution with the same shape parameter α and scale parameter β. It constitutes a two-parameter ensemble characterized by the shape parameter α and the scale parameter β [28].

$$f(x;\alpha,\beta) = \frac{\beta^\alpha}{\Gamma(\alpha)} x^{-(\alpha+1)} e^{(-\frac{\beta}{x})}, \quad x \geq 0 \tag{12}$$

Here, α is the same shape parameter as in the gamma distribution and β is the scale parameter, which is numerically equivalent to scale parameter $1/\beta$ of the gamma distribution. Similarly to what was explained in the previous subsection, it can be noted that a random variable X following the gamma distribution can also be considered a linearization of its reciprocal $Y = 1/X$, following an IG distribution.

Others

Apart from the previously considered PDFs, the log-normal, inverse-Gaussian, Landau, and Gibrat distributions all produced lower overall error cost than the gamma distribution, which had been identified as the best fit in earlier analyses. However, none of them outperformed the IG or IW distributions, so they are not considered further here.

Results and discussion

Evaluation methodology

After optimization and parameter estimation, the residual sum of squares (*RSS*) for each given distribution was calculated for each scenario by

$$RSS_n = \sum_i (m_n(\eta_i) - f_n(\eta_i))^2 \tag{13}$$

Here, $m_n(\eta_i)$ is the occurrence density and $f_n(\eta_i)$ is the estimated pdf at η_i for each measurement n. The *RSS* quantifies the deviation between the fitted model and the observed data, with lower values indicating a closer agreement. Consequently, *RSS* provides a direct measure of the goodness of fit and enables the identification of the most suitable distribution for modeling the precipitation clutter statistics. For every tested distribution, the mean of RSS_n for all measurements was calculated ($\overline{RSS}$). The standard error mean (*SEM*) is given by

$$SEM = \frac{\varsigma}{\sqrt{N}} \tag{14}$$

Here, ς is the standard deviation of RSS_n, and N is the number of measurements, in this case 26.

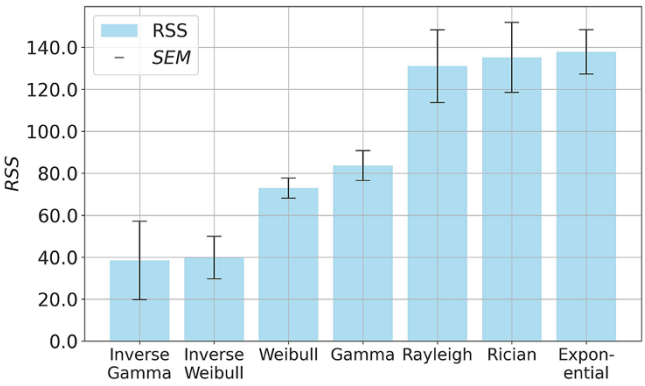


Figure 4. Error across distributions for R_{10}^{20}.

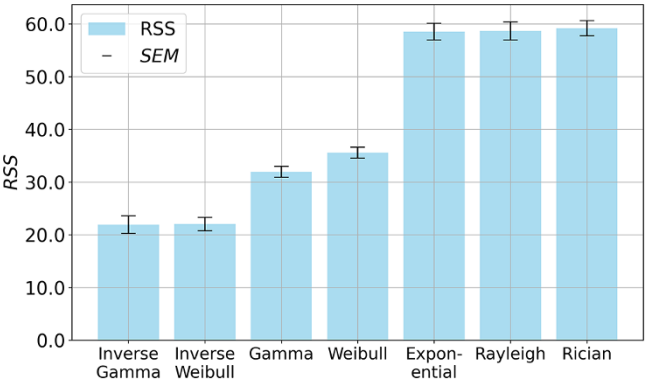


Figure 5. Validation of the proposed framework.

Model validation

Since the statistically best-fitting model across all evaluated scenarios is the IG distribution, as shown in Figure 4, a Monte Carlo verification was conducted to validate the proposed methodology. IG distributed datasets were generated, and the complete analysis pipeline, including adaptive binning and probability density fitting, was applied. This procedure was repeated for 50 independent realizations. The results, compared to the main considered PDFs, are shown in Figure 5. An overlap with the IW distribution is also observed, which is expected due to the similar heavy-tailed and positively skewed characteristics shared by both distributions. Nevertheless, the IG distribution was identified as the best-fitting model, demonstrating that the proposed binning and fitting framework reliably recovers the underlying distribution and does not introduce systematic bias.

To further quantify the goodness of fit, the Kolmogorov–Smirnov (KS) distance [29] between the empirical distribution and the fitted IG model was evaluated and found to be approximately 0.015. The KS distance measures the maximum deviation between the empirical and model cumulative distribution functions, with smaller values indicating closer agreement between the two. A KS distance this low is generally indicative of a good fit, suggesting that the fitted IG model closely captures the empirical distribution.

Characteristics of the baseline range

As mentioned in the fourth section, the key modeling is based on R_{10}^{20}, for which a comparison of *RSS* and *SEM* for all considered

https://doi.org/10.1017/S1759078726103055 Published online by Cambridge University Press

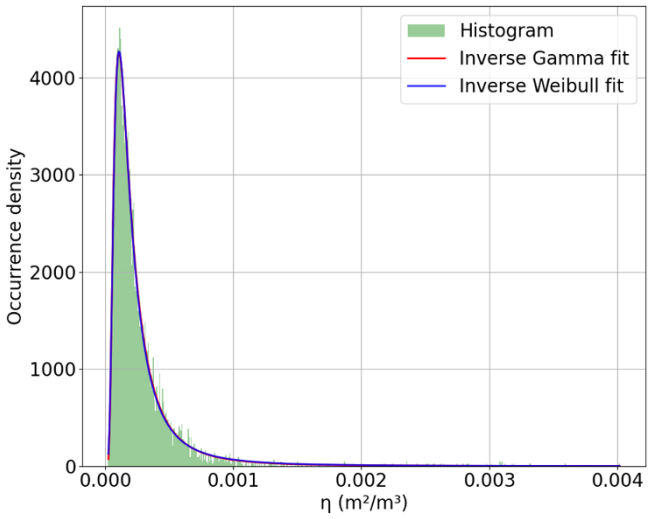


Figure 6. Histogram & model, TR 30 m, 32 mm/h.

distributions is provided in Figure 4. The bars indicate the *RSS* for each distribution, while the whiskers represent the *SEM*.

Applying the 1ς rule of the normal distribution, overlaps are observed among the exponential, Rician, and Rayleigh distributions, as well as between the Weibull and gamma, and between the IG and IW distributions. While IG and IW overlap and yield low errors, they remain separate from Weibull and gamma, outperforming them in histogram approximation. In comparison, Weibull and gamma still fit better than Rayleigh, Rician, and exponential distributions. Based on these observations, this study focuses on the IG and IW distributions.

The distinct numerical differences in parameters originate from different mathematical expressions of the two distributions, even though the fitted pdfs overlap substantially, as shown in Figure 6. The parameter variations across rain rates and spatial ranges are summarized in Figure 7. These results demonstrate that both IG and IW distributions exhibit similar behavior. The shape parameter remains within the same range (around 1.5–2.5), indicating the skewed and heavy-tailed nature of the data. In contrast, the scale parameter increases with rain rate (around 0.0002–0.002), indicating greater spread and higher reflectivity (η) in rain clutter back-scattering. This is consistent with the Marshall–Palmer drop size distribution, which predicts larger raindrop sizes at higher rain rates [15]. Although the dataset at 98 mm/h was smaller and less reliable due to measurement time limitations, its results are consistent with those at 16, 32, and 66 mm/h for R_{10}^{20}, showing the same trends in shape and scale.

Evaluation against earlier modeling approaches

The results obtained in this study are consistent with the tendencies reported in [1], where a gamma distribution was utilized instead of the IG model considered here. Although the two pdfs are different, their parameter characteristics show similar trends. This can be explained by the statement mentioned in "Inverse-Weibull (IW) distribution" and "Inverse-gamma (IG) distribution" of "Probability distribution functions" section, that the random variables of the gamma and Weibull distributions can be seen as linearization of the IG and IW variables. Since IG and IW provide the best fit, the gamma and Weibull offer quite reasonable, though limited, approximations. Additionally, the IG and IW distributions provide greater flexibility in capturing heavy-tailed behavior, making them advantageous for modeling rain clutter characteristics. The previous work removed outliers, whereas this study contained them while improving resolution in the dense region of the histogram. The validity of this approach is reflected in Figure 4, which shows markedly lower *RSS* values for the IG and IW models.

Spatial range dependent sensitivity

In this section, different intervals $[y_{\min},\ y_{\max}]$ were considered as ranges under test ($R_{y_{min}}^{y_{max}}$). The shape and scale parameters of both IG and IW models for different $R_{y_{min}}^{y_{max}}$ ranges are presented in Figure 7. As the range increases, the number of raindrop detections is reduced. $R_{y_{min}}^{y_{max}}$ windows with the common near bound y_{min} and far bounds extending by 1, 5, 10, and 20 m were examined. For moderately sized spatial ranges (e.g., 5 and 10 m), the estimated parameters exhibit substantial overlap and a clear dependence on rain rate.

In general, there is not much effect of different spatial ranges on the characteristics of the parameters of both models. However, for a narrow spatial range of 1 m, the scale parameter of both models is observed to increase sharply with rain rate. In contrast, for a wider spatial range of 30 m, the scale parameter still increases with rain rate but more gradually. These observations are up for discussion, as fewer detections may lead to a higher influence of outliers.

The authors suspect that these differences arise because the measured reflectivity parameter η from back-scattering by raindrops is inherently exponential. However, the analyzed data is

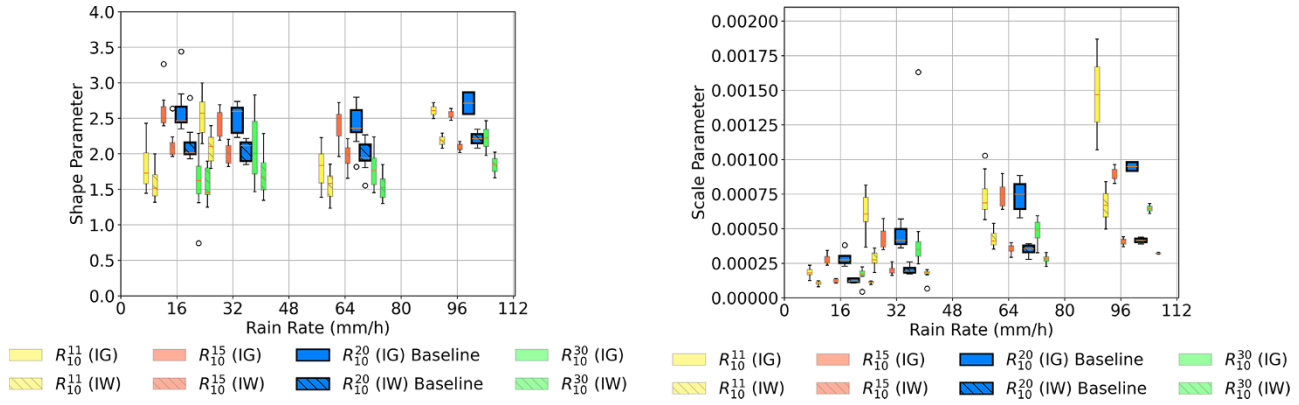


Figure 7. Best-fit model parameters across rain rates and spatial ranges.

https://doi.org/10.1017/S1759078726103055 Published online by Cambridge University Press

obtained from radar detection lists and is therefore influenced by the sensor's internal detection algorithm. This processing may include thresholding and range-dependent sensitivity effects, which may suppress weak signal components. As a result, the measured reflectivity statistics are biased by the radar hardware and detection settings. Consequently, the distribution of η deviates from a purely exponential form and is better described by gamma, IG, or IW models. Since cross-sensor validation is not available in this study, sensor-specific influences cannot be isolated. In [30], the impact of the sensor detection algorithm on rain backscattering distributions is investigated through simulation-based analysis. Future work will extend this effort by conducting cross-sensor comparisons to better understand the influence of radar characteristics and detection algorithms on rain clutter statistics.

Furthermore, the IW model exhibits similar parameter trends and data fitting quality as the IG model across ranges and rain rates, reinforcing empirical observations that both models effectively capture the heavy-tailed nature and variability of rain backscatter. The subtle differences in parameter estimates reflect inherent mathematical distinctions between the models but do not significantly affect their ability to describe the data distribution.

These statistics can be utilized to model rain clutter for various rain rates through interpolation. As already discussed in "Automotive radars" section, modeling automotive radar backscattering using Mie theory is particularly complex due to the absence of applicable approximations for these radars. Such models can be employed to test measurements for automotive radars in SiL- and HiL-setups, providing an empirical approach to modeling rain back-scattering.

Conclusion

This paper addresses the need for a rain clutter back-scattering model for automotive radar operating at 77 GHz. Although some research exists in this area, much remains unexplored. Radar measurements were conducted in an indoor facility using an irrigation system replicating the Marshall–Palmer drop size distribution. Data were processed using 3-layer robust adaptive binning, and optimized parameter estimation for 119 distributions was performed. The IG and IW distributions exhibited the lowest *RSS*. These results were further validated based on Monte Carlo simulations.

The shape and scale parameters of both best-fit models were analyzed across varying rain rates, revealing that the shape parameter remains nearly constant, whereas the scale parameter increases with increasing rain rate. These results were compared to the previous analysis reported in [1]. In addition, different spatial ranges were considered for the rain clutter back-scattering models, indicating that varying the spatial range from narrow to wide has minimal impact, with similar patterns observed across ranges. Such analyses can be used to model rain clutter back-scattering in SiL-, HiL-, and ViL-setups. These rain clutter models and test setups provide repeatable scenarios for further research and development in target detection, dynamic range enhancement, and noise reduction for ADAS radar systems.

In future work, the statistics derived from this study may be compared with and complemented by wind velocity distributions. The potential influence of a dominant reflector on rain clutter backscattering will also be investigated, providing insights into the effect of nearby vehicles on clutter characteristics. Furthermore, an outdoor rain measurement setup is being developed to enable more realistic characterization of rain clutter.

Acknowledgements. This paper was funded by the German Research Foundation (DFG) through the project "P2: Szenarien-basierte Testmethodik für die virtuelle Verifikation und Validierung von KFZ-Radaren" (project number 503852364). The measurement campaign was funded by the German Federal Ministry of Education and Research (BMBF) through project "Virtuelle Validierung – VIVID" (BMBF 16ME0164k). The authors would like to extend their heartfelt thanks to A. Schwind, and S. Buddappagari, former members of the RF and Microwave Research Group at Technische Universität Ilmenau, for conducting the measurements, preprocessing, and providing the data.

Competing interests. The authors report no conflict of interest.

References

1. **Gupta S, Varga I, Hein M and Dallmann T** (2025) Modelling of rain clutter based on empirical data for automotive radar validation. *19th European Conference on Antennas and Propagation,* 30 March–4 April 2025, Stockholm, Sweden. Piscataway, NJ, USA: IEEE. https://doi.org/10.23919/EuCAP63536.2025.10999978.
2. **Buddappagari S, Asghar M, Baumgärtner F, Graf S, Kreutz F, Löffler A, Nagel J, Reichmann T, Stephan R and Hein M** (2021) Over-the-air vehicle-in-the-loop test system for installed-performance evaluation of automotive radar systems in a virtual environment, pp. 278–281.
3. **Wald S, Mathy T, Nair S, Leon C and Dallmann T** (2020) ATRIUM: test environment for automotive radars.
4. **Rocha C, Ribeiro R, Cruz P and Viana P** (2019) Automatized solution for Over-the-Air (OTA). *2019 IEEE-APS Topical Conference on Antennas and Propagation in Wireless Communications (APWC)*, 09–13 September 2019, Granada, Spain. Piscataway, NJ, USA: IEEE, 370–374. https://doi.org/10.1109/APWC.2019.8870448.
5. **Sievers G, Seiger C, Peperhowe M, Krumm H, Graf S and Hanselmann H** (2018) Driving simulation technologies for sensor simulation in sil and hil environments.
6. **Skolnik MI** (2008) *Radar Handbook*, 3rd Edn. New York, NY, USA: The McGraw-Hill.
7. **Hobbs PV and Rangno AL** (2004) Super-large raindrops. *Geophysical Research letters* **31**(13). https://doi.org/10.1029/2004GL020167.
8. **ITU-R** (2005) Recommendation ITU-R P.838-2: specific attenuation model for rain for use in prediction methods.
9. **Zhao Z, Zhang M and Wu Z** (2001) Analytic specific attenuation model for rain for use in prediction methods. *International Journal of Infrared and Millimeter Waves* **22**(1), 113–120. https://doi.org/10.1023/A:1010717821659.
10. **Olsen R, Rogers D and Hodge D** (1978) The aR b relation in the calculation of rain attenuation. *IEEE Transactions on Antennas and Propagation* **26**(2), 318–329. https://doi.org/10.1109/TAP.1978.1141845.
11. **Gourova R, Krasnov O and Yarovoy A** (2017) Analysis of rain clutter detections in commercial 77 GHz automotive radar. 25–28.
12. **Jang B, Jung I, Soo Chong K, Sung H and Lim S** (2019) Rainfall observation system using automotive radar sensor for ADAS based driving safety. 305–310.
13. **Richard V, Kammerer J and Wallace H** (1988) Rain backscatter measurements at millimeter wavelengths. *IEEE Transactions on Geoscience and Remote Sensing* **26**(3), 244–252. https://doi.org/10.1109/36.3027.
14. **Technische Hochschule Ingolstadt** (2023) Online: https://www.thi.de/en/research/carissma/.
15. **Marshall J and Palmer W** (1948) The distribution of raindrops with size. *Journal of Atmospheric Sciences* **5**(4), 165–166. https://doi.org/10.1175/1520-0469(1948)005<0165:TDORWS>2.0.CO;2.
16. **ARS430 - Advanced Radar Sensor** (2024) Continental Engineering Services. Online: https://conti-engineering.com/components/ars430/.
17. **Freedman D and Diaconis P** (1981) On the Histogram as a Density Estimator: L 2 Theory. In *Zeitschrift für Wahrscheinlichkeitstheorie und Verwandte Gebiete* **57**(4), 453–476.
18. **Clauset A, Shalizi C and M Newman** (2009) Power-Law Distributions in Empirical Data. *SIAM Review* **51**(4), 661–703. https://doi.org/10.1137/070710111.

https://doi.org/10.1017/S1759078726103055 Published online by Cambridge University Press

19. **Cover Thomas M and Thomas Joy A** (1999) *Elements of Information theory, 9.3.* 1st Edn (1991). New York, NY, USA: John Wiley & Sons, Inc.
20. **Virtanen P, Gommers R, Burovski E, Oliphant T, Weckesser W, Cournapeau D, Peterson P, Reddy T, Haberland M and Wilson J, others** (2021) Geneva, Switzerland: Zenodo, CERN. https://doi.org/10.5281/zenodo.4718897.
21. **Gavin H** (2019) The Levenberg-Marquardt algorithm for nonlinear least squares curve-fitting problems. *Department of Civil and Environmental Engineering Duke University* **4**(3), 1–23. August, 3.
22. **Papoulis A and Pillai S** (2002) *Probability, Random variables, and Stochastic processes.*, New York, NY, USA: McGraw-Hill Europe.
23. **Blair W and Brandt-Pearce M** (1996) Estimation and discrimination for Swerling targets. 280–284.
24. **Richards M** (2008) Generating Swerling Random Sequences. Revised: August, 8.
25. **Van Valkenburg M** (2002) *Reference Data for Engineers: Radio, Electronics, Computers and Communications.* 9th Edn. Woburn, MA, USA: Butterworth-Heinemann.
26. **Babacan E** (2024) Bayesian estimation of inverse weibull distribution scale parameter under the different loss functions. *Sigma Journal of Engineering and Natural Sciences* **42**(4), 1108–1115. Yildiz Technical University.
27. **Hassan A and Nassr S** (2018) The inverse weibull generator of distributions: properties and applications. *Journal of Data Science* **16**(4), 723–742. https://doi.org/10.6339/JDS.201810_16(4).00004.
28. **Cook J** (2008) Inverse gamma distribution. Online: http://www.johndcook.com/inversegamma.pdf, Technical. Report.
29. **Stephens MA** (1974) EDF statistics for goodness of fit and some comparisons. *Journal of the American Statistical Association* **69**(347), 730–7.
30. **Gupta S and Dallmann T** (2026) Simulation and validation study of rain scattering effects in 77 GHz automotive radar. *20th European Conference on Antennas and Propagation*, 19–24 April 2026, Dublin, Ireland. Piscataway, NJ, USA: IEEE.



Sonakshi Gupta earned her Bachelor of Technology in Electronics and Communication Engineering from Guru Nanak Dev University, Amritsar, India, in 2018 and her Master of Science in Communication and Signal Processing from Technische Universität Ilmenau in 2022. She is currently a Research Scientist in the Radio Technologies for Automated and Connected Vehicles group at the Thüringer Innovationszentrum Mobilität (ThIMo). Her work focuses on statistical modeling, advanced driver-assistance sensor validation, and sensor virtualization for simulation and testing environments.



Isabella Varga received the B.Sc. and M.Sc. degrees in electrical engineering and information technology from Technische Universität Ilmenau, Ilmenau, Germany, in 2021 and 2023, respectively. She is a Research Scientist in the RF and Microwave Research Group at the Thüringer Innovationszentrum Mobilität, working in the field of radar technologies for automotive applications. Her current research focuses on radar signatures of extended targets based on reflectivity measurements, including modeling, calibration techniques, and signal processing.



Matthias A. Hein (Diploma in Physics 1987, Doctoral dissertation on microwave superconductivity, Dr. rer. nat. 1992, Habilitation 1998) began his academic career at the University of Wuppertal, Germany, researching superconductors for mobile and satellite communications. Following a 13-month British EPSRC Senior Research Fellowship at the University of Birmingham, he joined TU Ilmenau in 2002 as head of the RF and Microwave Research Laboratory. He established the multi-purpose automotive antenna test range "VISTA – Virtual Road Simulation and Test Area" at the Thuringian Center of Innovation in Mobility (ThIMo). His research focuses on antennas and microwaves for intelligent automotive wireless sensor and communication systems, over-the-air testing, and virtual test drives. He has co/authored over 650 publications, delivered over 70 invited talks, and supervised 48 doctoral, 102 master's, and 91 undergraduate projects, attracting nearly 25 MEUR in research funding. A VDE member since 2003 and an IEEE Senior Member since 2006, he became Director of ThIMo at TU Ilmenau in 2021.



Thomas Dallmann received the Dipl.-Ing. degree in electrical engineering from the RWTH Aachen University, Germany, in 2010 and the Dr.-Ing. degree from the same institution in 2017. From 2016 to 2022, he was with the Fraunhofer-Institute for High Frequency Physics and Radar Techniques FHR, Wachtberg, Germany and led a research group in Aachen, Germany. He is currently Junior Professor at Technische Universität Ilmenau, Germany and is responsible for the Radio Technologies for Automated and Connected Vehicles Research Group. His research is concerned with joint communication, radar sensing networks, and virtual validation of automotive radars.

https://doi.org/10.1017/S1759078726103055 Published online by Cambridge University Press